Advanced Materials

ADVANCED MATERIALS
www.advmat.de

RESEARCH ARTICLE

Elastic Bridging Design of a Fluorine-Free Electrolyte Enables High-Performance Lithium Batteries

Shi Wang[1,2] | Wenqing Sun[1] | Bo Zhang[3] | Jiazhu Guan[4] | Tong Wu[1] | Fangqi Zhan[1] | Dalin Wang[1,5] | Shoubin Zhou[1,5] | Qian Wang[3] | Zhong Jin[2] | Wen-Yong Lai[1]

[1]State Key Laboratory of Flexible Electronics (LoFE), Institute of Advanced Materials (IAM), School of Chemistry and Life Sciences, Nanjing University of Posts and Telecommunications, Nanjing, Jiangsu, China | [2]State Key Laboratory of Coordination Chemistry, MOE Key Laboratory of Mesoscopic Chemistry, MOE Key Laboratory of High Performance Polymer Materials and Technology, Jiangsu Key Laboratory of Green Energy Catalysis and Intelligent Chemical Engineering, Suzhou Key Laboratory of Green Intelligent Manufacturing of New Energy Materials and Devices, Tianchang New Materials and Energy Technology Research Center, Institute of Green Chemistry and Engineering, School of Chemistry and Chemical Engineering, Nanjing University, Nanjing, Jiangsu, China | [3]College of Materials Science and Engineering, Taiyuan University of Technology, Taiyuan, Shanxi, China | [4]School of Chemical Sciences, University of Chinese Academy of Sciences, Beijing, China | [5]Nanjing University of Posts and Telecommunications and Huafu (Jiangsu) Lithium New Technology Co., Ltd., Gaoyou, Jiangsu, China

Correspondence: Shi Wang (iamshiwang@njupt.edu.cn) | Qian Wang (qianwang0825@pku.edu.cn) | Zhong Jin (zhongjin@nju.edu.cn) | Wen-Yong Lai (iamwylai@njupt.edu.cn)

Received: 7 January 2026 | **Revised:** 17 March 2026 | **Accepted:** 23 March 2026

Keywords: fluorine-free lithium salt | fluorine-free polymer electrolyte | interfacial stability | ionic conductivity | Li metal batteries

ABSTRACT

The escalating demand for lithium-based batteries has underscored the urgency to address safety and environmental risks associated with conventional electrolytes. To mitigate these challenges, we propose a fluorine-free electrolyte architecture leveraging tailored solvent-polymer elastic bridging. This design encapsulated LiBOB-based F-free localized high-concentration electrolyte within an elaborately synthesized zwitterionic polyurethane combining rigid-flexible molecular motifs. The chain-solvent elastic bridging strategy reconstructs the solvation environment through selective Li^+-solvent coordination, while modulates weak intermolecular interactions in the polymer backbone to guide ion transport and further improve mechanical properties. Thus, the resultant fluorine-free electrolyte achieves an extremely high lithium-ion transference number of 0.95, high room-temperature ionic conductivity of 1.3 mS cm^{-1} and high fracture strength of 1.1 MPa. These advancements synergize with the formation of an inorganic boride-rich interfacial layer, enabling Li||Li symmetric cells to sustain plating/stripping of 1000 h. Moreover, solid-state full cells achieve superior performance; for instance, the Li|| NCM622 (10 mg cm^{-2}) cell exhibits an average capacity of 1.6 mAh cm^{-2} (140 mAh g^{-1}) and a coulombic efficiency of 99.4% over 200 cycles, and a pouch cell also achieves a capacity of 1600 mAh. This work pioneers electrolyte design innovation through molecular solvent-polymer synergy and macroscopic electrochemical integration, enabling sustainable fluorine-free energy storage commercialization.

Shi Wang, Wenqing Sun, Bo Zhang, and Jiazhu Guan contributed equally to this work.

1 | Introduction

Lithium-ion batteries (LIBs) now dominate the electric vehicle and consumer electronics sectors and play a pivotal role in grid-scale advanced energy storage systems [1], while lithium metal batteries (LMBs) are going to commercialization as next-generation energy storage solutions due to their superior theoretical energy density [2, 3]. However, due to the electrolyte's flammability and its tendency to induce unstable solid electrolyte interphase (SEI) film formation on the lithium anode, which accelerates lithium dendrite growth, LMBs pose significant safety hazards. High-concentration electrolytes (HCEs) and localized high-concentration electrolytes (LHCEs) have demonstrated significant advantages in enhancing lithium metal interface stability [4]. Notably, LHCEs incorporating nonpolar diluents exhibit higher room-temperature ionic conductivity and lower costs [5]. However, LHCEs also present risks of flammability and liquid leakage, thereby remaining inadequate in ensuring the safety of LMBs [6–8]. Furthermore, LHCEs not only require fluorinated lithium salts similar to other electrolytes but even necessitate high-cost fluorinated diluents. Thus, scaling up such technology intensifies environmental concerns [9–15]. A more critical issue is that while LHCEs exhibit high ionic conductivity at room-temperature, their effective lithium-ion transference number remains significantly low due to insufficient anion immobilization. This deficiency severely restricts battery cycle life. At present, gel polymer electrolytes (GPEs) prepared by gelatinizing liquid electrolytes represent an effective strategy to enhance the safety of LMBs [16–23].

Therefore, developing fluorine-free LHCEs and encapsulating them within polymer networks to construct fluorine-free GPEs holds promise for addressing the aforementioned challenges. However, the development of fluorine-free LHCEs remains scarcely reported and highly challenging, primarily due to two fundamental constraints: (1) the intrinsically limited solubility of fluorine-free lithium salts in organic solvents (while $LiClO_4$ exhibits high solubility, its strong oxidizing nature and thermal instability severely hinder practical applications [24–26]) [27–29], and (2) the thermodynamic instability of solvation structures within fluorine-free lithium salt electrolyte systems [30]. Furthermore, even when solubility enhancement strategies are employed, realizing stable liquid—phase encapsulation of these electrolytes proves to be an exceptionally arduous task. The root cause lies in the persistent difficulty of achieving precise and sophisticated modulation of the intermolecular interactions that occur between solvent molecules and polymer chains, which remains an unsolved puzzle in the cutting-edge field of electrolyte research. More gravely, akin to the long-standing and intractable challenge encountered in conventional gel electrolytes, the realization of a high lithium-ion transference number within fluorine-free gel systems persists as a formidable scientific and engineering conundrum that demands in-depth exploration and innovative solutions [31–35].

Herein, leveraging a solvent-polymer elastic bridging strategy, which entails the establishment of hydrogen bonding and ion-dipole interactions between the solvents of a fluorine-free LHCE and the chains of a fluorine-free polymer, we develop a fluorine-free GPE with single-ion conducting for sustainable LMBs. Specifically, we designed and prepared for the first time a LiBOB-based tetraethylene glycol dimethyl ether (T, strong coordination)/γ-valerolactone (V, weak coordination) fluorine-free LHCE. This fluorine-free LHCE was further encapsulated within an elaborately designed zwitterionic polyurethane to construct a novel fluorine-free solvent-polymer elastic bridging GPE. Through hydrogen bonding and ion-dipole interactions between the zwitterionic polyurethane and solvent molecules, solvents-Li^+ coordination in the fluorine-free LHCE is further weakened, not only achieving solvent encapsulation but also promoting the formation of rich anion-dominated solvation structures. Moreover, by leveraging the synergistic effect of rigid and flexible components in the zwitterionic polyurethane backbone, combined with weak intermolecular interactions, the electrolyte is endowed with elasticity, self-healing capability, and forms zwitterionic nanochannels for efficient lithium-ion transport. As a result, the fluorine-free GPE exhibits outstanding mechanical and electrochemical performances, especially, an extremely high lithium-ion transference number of 0.95 is achieved. Further combined with the inorganic boride-rich interfacial layer, the assembled batteries demonstrate superior rate performance and long-cycle stability. This work pioneers a new paradigm for the practical application of fluorine-free GPEs.

2 | Results and Discussion

Taking into comprehensive consideration the thermal stability, electrochemical stability, safety, cost, and other factors of fluorine-free lithium salts, LiBOB emerges as a relatively ideal fluorine-free lithium salt. Therefore, in this work, LiBOB was selected as the sole lithium salt to develop a fluorine-free LHCE, which was then encapsulated within a fluorine-free polymer to prepare a fluorine-free polymer-based electrolyte. To prepare the fluorine-free LHCE, LiBOB was dispersed in T, followed by added V. As clearly demonstrated in Figure S1, the T-Li mixture appeared mildly turbid, whereas the T-V-Li system became transparent after adding V. Additionally, the V-Li mixture remained significantly turbid. These observations confirm that the strong-weak coordination between T, V, and lithium ions effectively enhances the solubility of LiBOB. Subsequently, a zwitterionic polyurethane was synthesized via polycondensation reaction (Scheme S1), the ^1H NMR spectrum in Figure S2 confirm the successful synthetic of the polymer. The polymer is then combined with the fluorine-free electrolyte (T-V-Li) to yield a fluorine-free zwitterionic polyurethane electrolyte (TPU-T-V-Li). Scheme 1 illustrates the design concept of TPU-T-V-Li: the unique rigid-flexible components and intermolecular hydrogen bonding within the zwitterionic polyurethane structure endow the electrolyte with exceptional elasticity and efficient self-healing capability. Within the polymer network, strong coordination interactions exist between LiBOB and T, while weak coordination occurs with V. Furthermore, hydrogen bonding interactions between the -NH- groups in zwitterionic polyurethane with both T and V contribute to weakening solvent-lithium ion coordination, promoting the formation of rich anion-derived solvation structures and facilitating further lithium ion desolvation. Free lithium ions are subsequently rapidly transported within the zwitterionic nanochannels, achieving high ionic conductivity for the fluorine-free polymer electrolyte system.

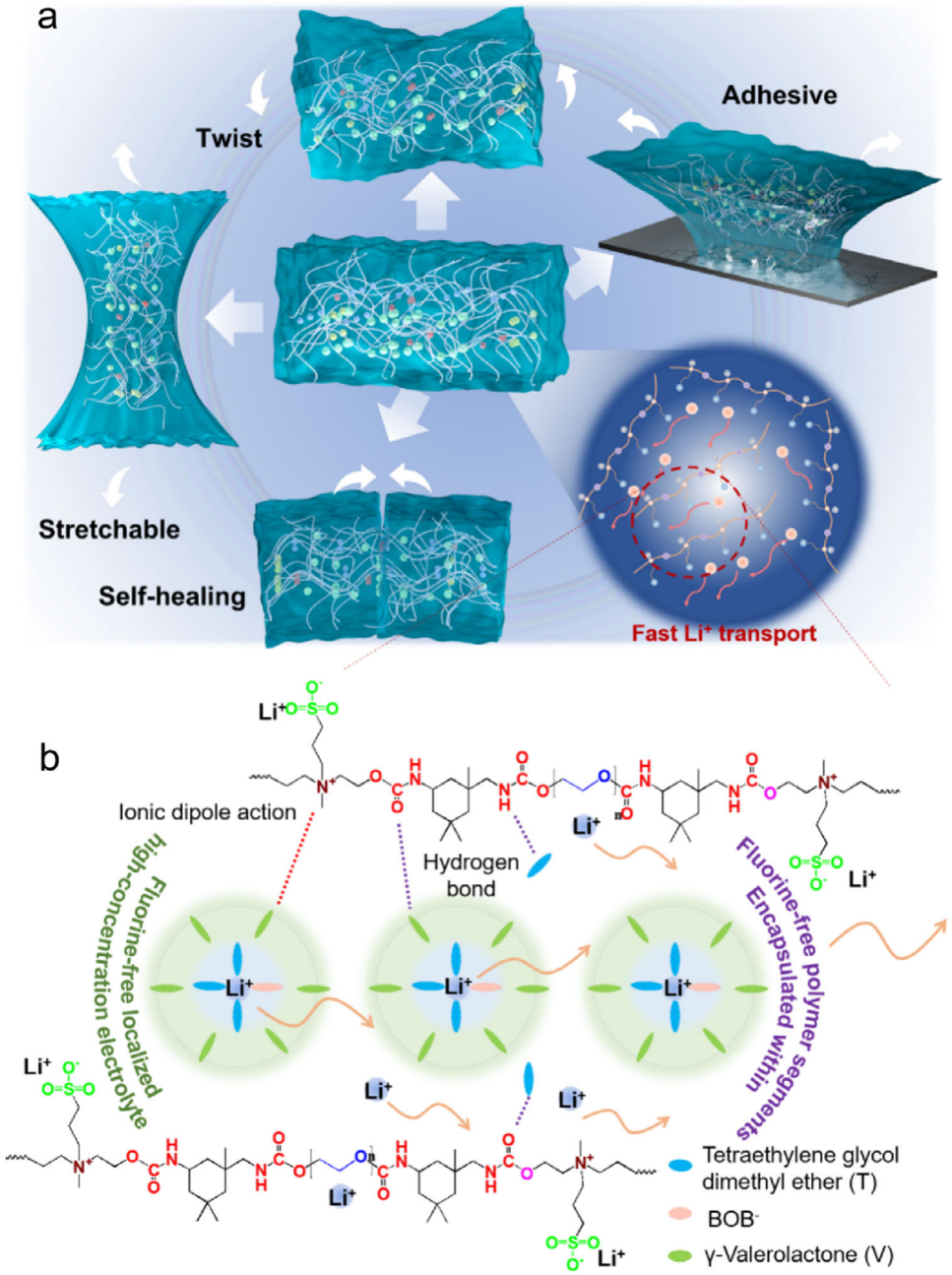

SCHEME 1 | Electrolyte multifunctionality and interaction mechanism: (a) Schematic illustration of the multifunctional properties of the fluorine-free zwitterionic polyurethane electrolyte. (b) Interaction mechanism between solvent, polymer segments, and LiBOB of the designed elastic fluorine-free zwitterionic polyurethane electrolyte.

The good thermal stability of TPU (Figure S3a) and TPU-T-V-Li (Figure S3b) was confirmed through TGA analysis. DSC measurements revealed that TPU-T-V-Li exhibits a significantly lower glass transition temperature (T_g) (Figure S3c, -53.7°C) compared to TPU (Figure S3d, -46.6°C), suggesting that T-V-Li incorporation enhances polymer chain mobility and can consequently improve ionic conductivity. The interactions among different components of the electrolyte were initially investigated using IR spectroscopy. The addition of V to LiBOB induced noticeable shifts in the characteristic vibrational peaks of the C═O (Figure 1a) and O—B—O ring (Figure 1b) within the BOB^- anion. Notably, Figure 1a demonstrates that the C═O stretching vibration in V underwent a redshift from 1768 to 1761 cm^{-1}. Furthermore, when T was introduced into the LiBOB system, significant spectral shifts were observed for key functional groups in the BOB^- anion, including O—B—O and C—O—C vibrations (Figure 1c). Specifically, the characteristic C—O—C stretching peak associated with T exhibited a red shift from 1029 to 1017 cm^{-1}, likely due to strong lithium ion coordination with T. A comparative analysis reveals that LiBOB induces a more pronounced shift in the C—O—C peak of T compared to its effect on the C═O shift in V, suggesting a stronger coordination interaction between lithium ions and the C—O—C functional groups.

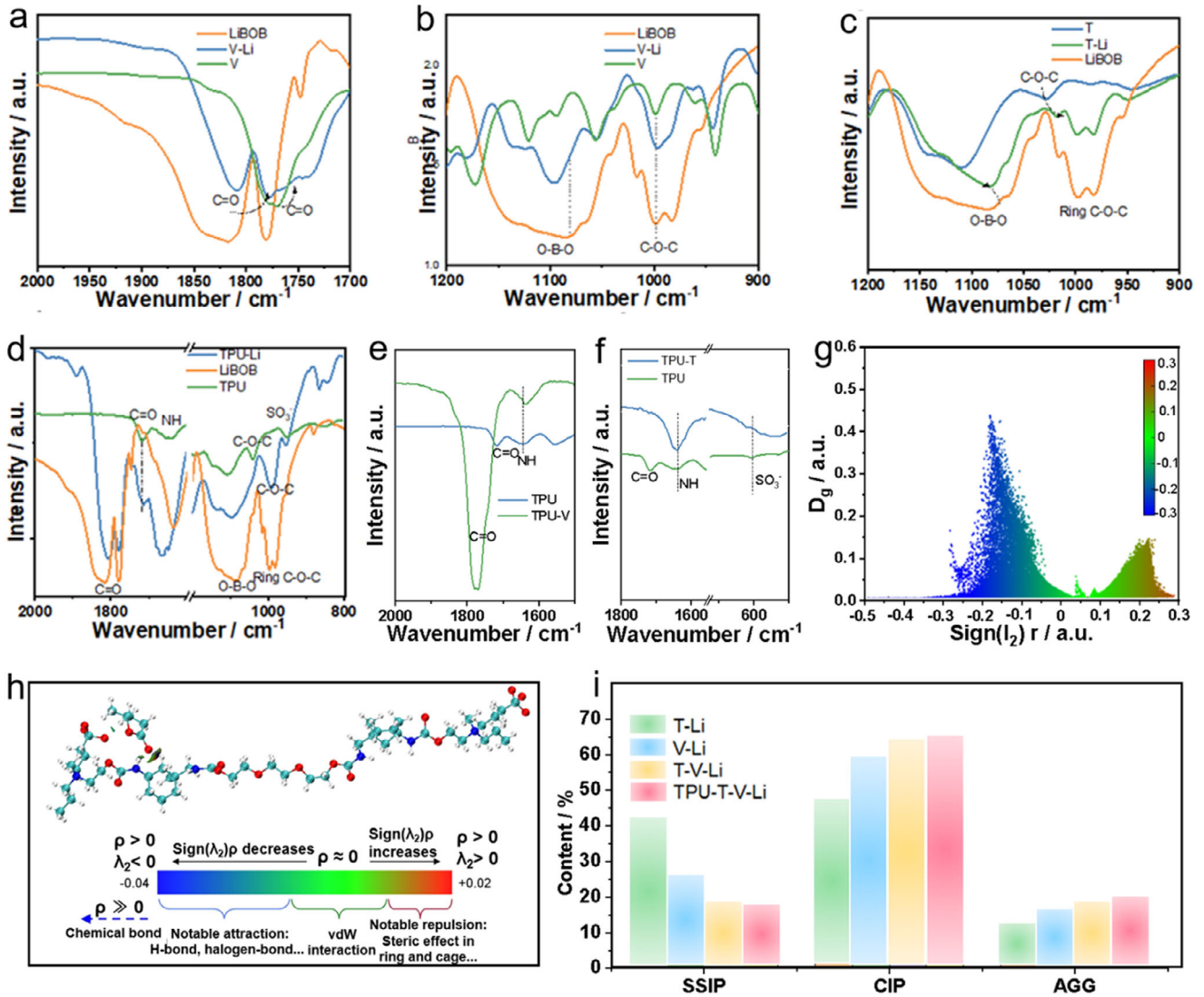

FIGURE 1 | Characterization of intermolecular interactions in electrolytes. (a–c) IR spectra of LiBOB and various prepared fluorine-free liquid electrolytes. (d) IR spectra of LiBOB, amphoteric polyurethane, and TPU-Li. (e) IR spectra of TPU and TPU-V. (f) IR spectra of TPU and TPU-T. (g,h) Verify the intermolecular hydrogen bond interaction based on the Independent Gradient model (IGM). (i) The content of SSIP, CIP, and AGG in various prepared electrolytes.

Figure 1d further explores the interaction between TPU and LiBOB. Notably, the characteristic C═O stretching vibration (1719 cm^{-1}) attributed to the TPU exhibits a red shift to 1715 cm^{-1} upon LiBOB addition, while the C═O peak (1819 cm^{-1}) from LiBOB itself also shifts to 1806 cm^{-1} after TPU incorporation. These spectral changes indicate mutual interactions between the polymer's C═O groups and lithium ions. The greater red shift observed for the TPU-derived C—O—C peak compared to the TPU–derived C═O peak upon LiBOB addition suggests preferential lithium ion coordination with C—O—C moieties. Additionally, the involvement of SO_3^- groups in TPU with lithium ions induces a characteristic red shift, which facilitates lithium ion transport through the zwitterionic nanochannels.

As shown in Figure 1e, hydrogen bonding interactions between V's C═O and TPU's NH groups cause a significant blue shift of the NH stretching band (from 1643 to 1631 cm^{-1}) following V incorporation. Similarly, Figure 1f reveals that introducing T into TPU leads to a redshift of the NH peak (from 1645 to 1638 cm^{-1}) due to hydrogen bonding with T's oxygen atoms. Concurrently, electrostatic interactions between the positively polarized carbon in C—O groups and SO_3^- anions induce a blueshift of the SO_3^- asymmetric stretching mode (from 603 to 617 cm^{-1}). Independent Gradient Model (IGM) analysis (Figure 1g,h) visually confirms the presence of hydrogen bonding interactions between monomers (such as V) and TPU chains, consistent with the IR spectroscopic observations.

Raman spectroscopy was further employed to analyze ionic aggregation patterns in these electrolyte systems and the fluorine-free zwitterionic TPU-based electrolytes (Figure S4). As depicted in Figure 1i, the V-Li complex exhibits markedly reduced solvent-separated ion pair (SSIP) populations compared to T-Li systems, with concurrent increases in contact ion pairs (CIP) and aggregates (AGG). The locally high-concentration T-V-Li system shows further suppression of SSIP species and enhanced

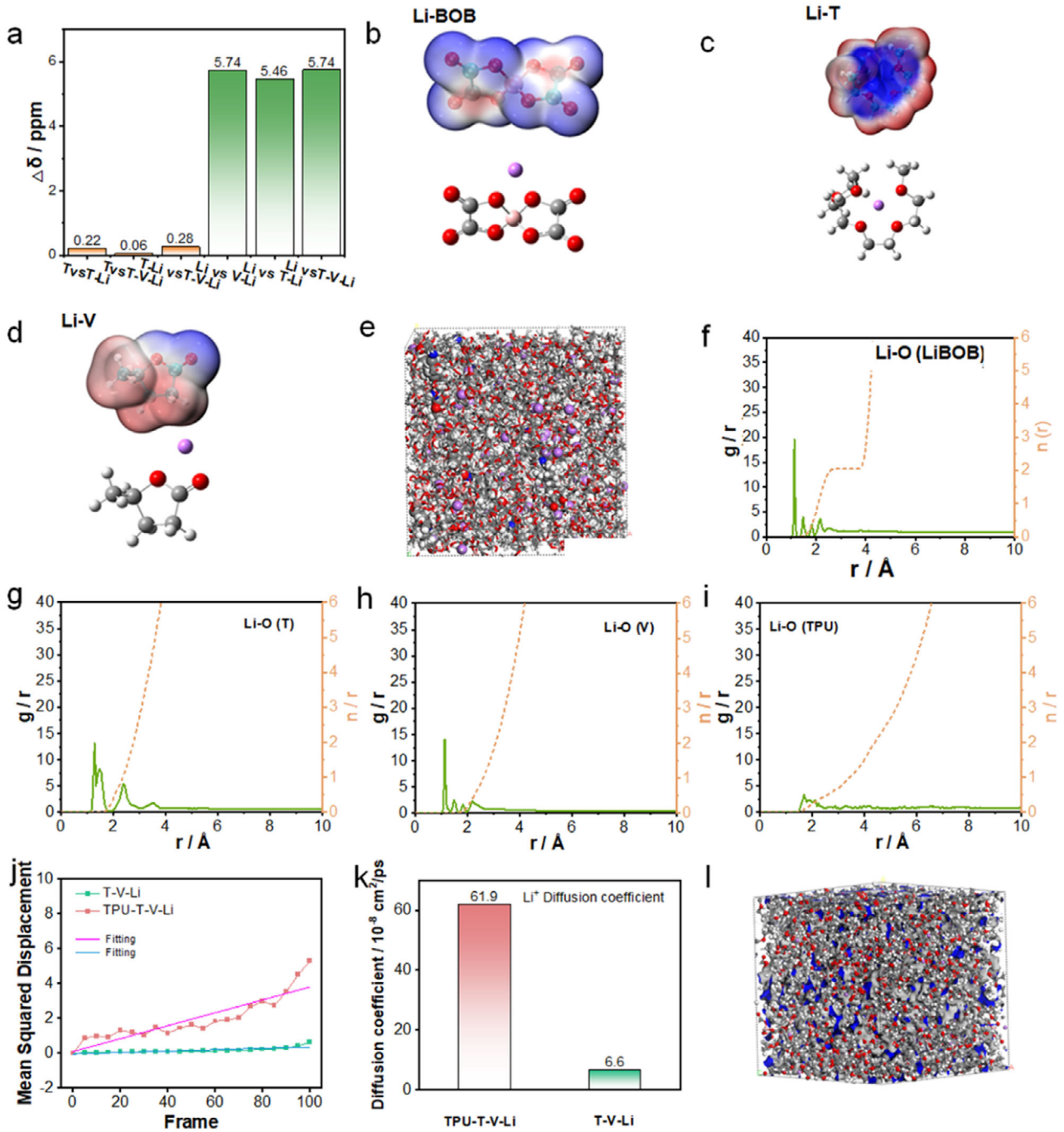

FIGURE 2 | Solvation structure and coordination of electrolytes. (a) Relative chemical shift variations of the terminal carbon in T (referenced to the terminal carbon) after introducing different components (samples: T vs. T-Li, T-Li vs. T-V-Li, T vs. T-V-Li), and relative chemical shift variations of the carbonyl carbon in LiBOB (referenced to the carbonyl carbon in LiBOB) after introducing different components (samples: Li vs. V-Li, Li vs. T-Li, Li vs. T-V-Li). Binding energies between Li^+ and (b) BOB^- anion, (c) T, and (d) V, respectively. (e) Snapshots of TPU-T-V-Li from molecular dynamics (MD) simulation. (f–i) Radial distribution functions (RDFs) in TPU-T-V-Li. (J) Mean squared displacement (MSD) of Li^+ in TPU-T-V-Li and T-V-Li. (k) Diffusion coefficients of Li^+ in TPU-T-V-Li and T-V-Li. (l) Simulated structure of TPU-T-V-Li.

CIP/AGG formation. Upon TPU incorporation, the solvent matrix demonstrates a slight increase in CIP/AGG content, indicating that the polymer network enables fine-tuning of lithium ion solvation structures.

Figure 2a illustrates the spectral shifts observed in characteristic ^{13}C NMR peaks for electrolyte components (the complete spectra are presented in Figures S5–S9, while the coordination interactions between Li^+ and solvent molecules are shown in Figure S10). The terminal carbon chemical shift of T is 58.61 ppm. Upon coordination with Li to form the T-Li complex, its chemical shift increases to 58.83 ppm ($\Delta = 0.22$ ppm), indicating that the strong polarization effect of Li^+ reduces the electron cloud density of the terminal oxygen in T (deshielding effect). When the weakly coordinating solvent V is further introduced to form the T-V-Li system, the terminal carbon chemical shift of T decreases to

58.59 ppm (Δ = 0.06 ppm), suggesting that V partially weakens the direct interaction between T and Li^+ through competitive coordination and dilution effects. Notably, the chemical shift difference between T-Li and T-V-Li (0.25 ppm) is slightly larger than that between T and T-Li (0.22 ppm), indicating that the addition of V does not completely disrupt the coordination between T and Li^+. Instead, it may slightly enhance the local coordination effect by adjusting the solvent structure (e.g., forming a T-Li^+-V complex). In LiBOB, the chemical shift of the C═O carbon on the B—O—B ring is 164.145 ppm. Upon coordination with T to form T-Li, its shift significantly decreases to 158.68 ppm (Δ = 5.462 ppm), demonstrating that the strong coordination capacity of T effectively stabilizes the electronic structure of BOB^-. The addition of V in the V-Li system reduces the C═O carbon shift to 158.416 ppm (Δ = 5.735 ppm), with a slightly larger difference compared to the T-Li system. This indicates that the weak coordination ability of V does not significantly stabilize BOB^-; instead, it intensifies the fluctuation of BOB^-'s electron cloud density due to the weak interaction between Li^+ and V. Interestingly, in the T-V-Li system, the C═O carbon shift further decreases to 158.404 ppm (Δ = 5.741 ppm), with a marginally increased difference. This suggests that the dilution effect of V does not interfere with the coordination between T and Li^+ but optimizes the solvation structure of Li^+ through synergistic effects, leading to a more stabilized electronic environment for BOB^-. Therefore, the strong coordination between T and Li^+ serves as the core mechanism of the LHCE. Meanwhile, V, acting as a weakly coordinating diluent, not only weakens the excessive coordination between T and Li^+ through competitive coordination and solvent structure adjustment but also maintains the relative stability of BOB^-. This further supports the formation of the locally high-concentration T-V-Li electrolyte. The binding energy calculations (E_b) show the following coordination hierarchy: E_b (Figure 2b, Li-T = 5.32) > E_b (Figure 2c, Li-BOB = 5.23) > E_b (Figures 2d, V-Li), further indicating lithium ions prioritize T coordination before engaging with V or BOB^- anions.

Molecular dynamics (MD) simulations were employed to investigate the solvation structures of the prepared electrolytes. In T-V-Li (Figure S11), the Li^+-O coordination numbers are 2.16 (T-Li), 1.17 (Li-BOB), and 0.65 (V-Li). Figure 2e shows the snapshots of T-V-Li-TPU from the MD simulation. Specifically, after TPU addition (Figure 2f–i), the Li^+-BOB^- coordination number increases to 1.37, while solvent coordination numbers decrease to 2.04 (T) and 0.32 (V). Notably, TPU fragments exhibit 0.24 Li^+ coordination, confirming their role in weakening Li^+-solvent interactions while strengthening Li^+-BOB^- binding. These findings align with both Raman spectroscopic and ^{13}C NMR observations, establishing a consistent picture of solvation structure modulation through component interactions.

Following equilibrium attainment in the simulated system, the mobility of Li^+ was evaluated through analysis of its mean square displacement (MSD) derived from molecular dynamics trajectories (Figure 2j). Notably, as shown in Figure 2k, the self-diffusion coefficient determined for Li^+ in the novel TPU-T-V-Li formulation (61.9×10^{-6} $cm^2 \cdot s^{-1}$) exhibits a nine-fold enhancement compared to the T-V-Li electrolyte benchmark (6.6×10^{-6} $cm^2 \cdot s^{-1}$). This pronounced kinetic advantage in the TPU-based electrolyte can be attributed to reduced solvation sheath energy around Li^+ and well-established ion channels via TPU, which facilitates greater ionic mobility through diminished ion-solvent interactions and ion transport energy barrier. Furthermore, in comparison to the simulated structure of T-V-Li (Figure S12), TPU-T-V-Li (Figure 2l) exhibits a significantly reduced solvent content outside the solvation radius, with more uniform dispersion and effective confinement of ionic species within the polymer networks.

The electrolyte membrane displays distinct phase-separated morphological characteristics at the microscale (Figure 3a), which facilitate efficient ion transport [36, 37]. The electrolyte film demonstrates an exceptional strain capacity of ~900% under 1.1 MPa stress (Figure 3b). This remarkable performance can be attributed to the synergistic effects of regulatory rigid-flexible segment ratios in the polymer matrix, intermolecular hydrogen bonding networks, ion-dipole interactions, and dynamic crosslinking between solvent molecules and polymer chains. As vividly illustrated in Figure 3c, the film exhibits extraordinary stretchability. The cyclic stress–strain curves and sequential tensile loading–unloading curves of TPU-T-V-Li collectively demonstrate its excellent elastic recovery properties (Figure 3d–f). Microscopic characterization reveals the electrolyte membrane's capability for effective self-healing at room-temperature within 5 h after fracture, as depicted in Figure 3g. This autonomous repair characteristic arises from the reversible nature of hydrogen bonding and ion-dipole interactions between polymer chains, and also weak interactions between polymer and compositions from T-V-Li (Figure 3h), enabling dynamic reconstruction of the material network. Notably, the TPU-T-V-Li system demonstrated exceptional interfacial adhesion performance when paired with a hydrophobic PET substrate. Under a contact area of 10 cm^2, an adhesive strength of 2.7 MPa was achieved. This finding highlights the material's potential for applications requiring robust mechanical interlocking at minimal contact interfaces. Moreover, the actual adhesion strength between the electrolyte membrane and metal electrode exceeds 6 N, as demonstrated in Figure 3k,l.

Figure 4a demonstrates that the high-concentration strongly solvating electrolyte T-Li exhibits higher room-temperature (RT) ionic conductivity (0.22 mS cm^{-1}) compared to the weakly solvating electrolyte V-Li (0.094 mS cm^{-1}), while the locally high-concentration V-T-Li electrolyte achieves further enhancement in RT ionic conductivity (0.85 mS cm^{-1}). These findings align with the preceding spectroscopic characterizations and theoretical calculations. After combining V-T-Li with TPU, a fluorine-free zwitterionic TPU electrolyte was successfully prepared, showing RT ionic conductivity of 1.3 mS cm^{-1}. Nonlinear (Figure 4b) and linear (Figure S13) fitting analyses were performed on the conductivity-temperature relationship of TPU-T-V-Li, with the nonlinear fitting exhibiting a superior goodness-of-fit (R^2 closer to 1), indicating lithium-ion transport better conforms to the Vogel–Tamman–Fulcher (VTF) model. The fitting results reveal two key aspects: (1) an activation energy of 1.33 kJ mol^{-1}, significantly lower than previously reported values [38, 39], and (2) plasticizers primarily interact with polymer chains through weak interactions, establishing a pseudofully polymerized ionic conduction mechanism. Furthermore, chronoamperometry and impedance spectroscopy analyses (Figure 4c) demonstrate that the TPU-T-V-Li electrolyte achieves a lithium-ion transference number of

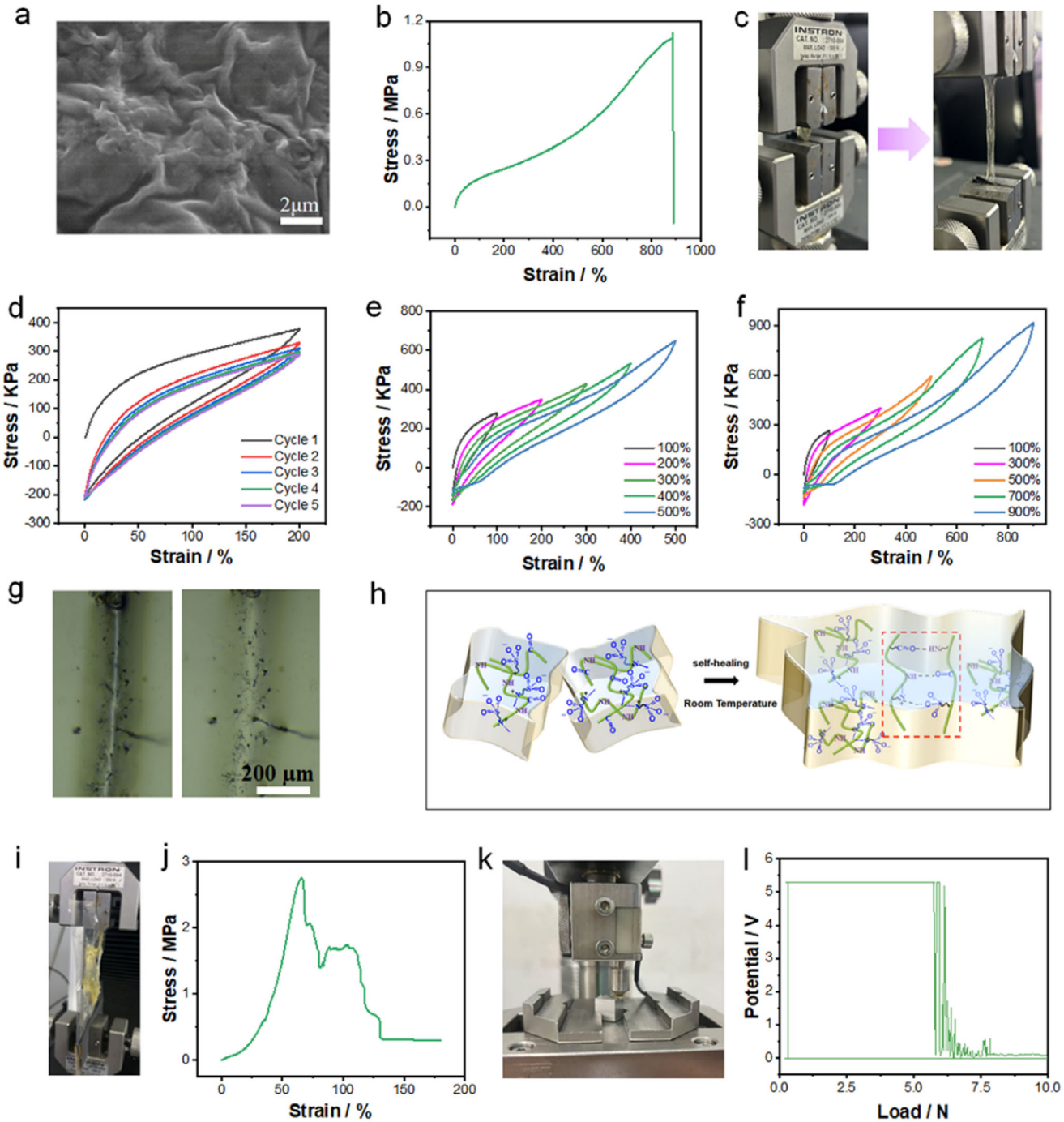

FIGURE 3 | Morphology and mechanical properties of electrolyte. (a) SEM image of TPU-T-V-Li. (b) Strain–stress curve of TPU-T-V-Li and (c) the corresponding physical object images before and after stretching. (d) Cyclic stress–strain curves of TPU-T-V-Li under continuous loading–unloading cycles without intervals at fixed strain ($\lambda = 2$) and constant tensile speed (v = 10 mm/min). (e,f) Sequential tensile loading–unloading curves of TPU-T-V-Li at different strain levels. (g) POM images of TPU-T-V-Li before and after self-healing. (h) Self-healing mechanical of TPU-T-V-Li. (i) Adhesion test and its (j) physical diagram. (k) Real adhesion test photograph and (l) adhesion test curve.

0.95, substantially exceeding 0.41 for T-V-Li (Figure S14) and 0.5 for commercial electrolytes (Figure S15). This observation correlates with molecular dynamics simulations of lithium-ion diffusion coefficients, further underscoring the critical synergistic effects of reduced lithium-ion migration barriers in the T-V-Li electrolyte system and the zwitterionic nanochannel architecture in facilitating lithium-ion transport. The LSV curve in Figure 4d confirms that the TPU-T-V-Li electrolyte exhibits an electrochemical window exceeding 4.8 V, which provides a critical safety margin for high-voltage cathode operation. DFT calculations reveal that T-Li (-10.36 eV) and V-Li (-13.2 eV) exhibit lower highest occupied molecular orbital (HOMO) energies compared to Li-BOB (-8.42 eV), attributed to the electron-withdrawing effects of ether and ester groups, which significantly enhance the antioxidant capability of the developed electrolyte system (Figure 4e).

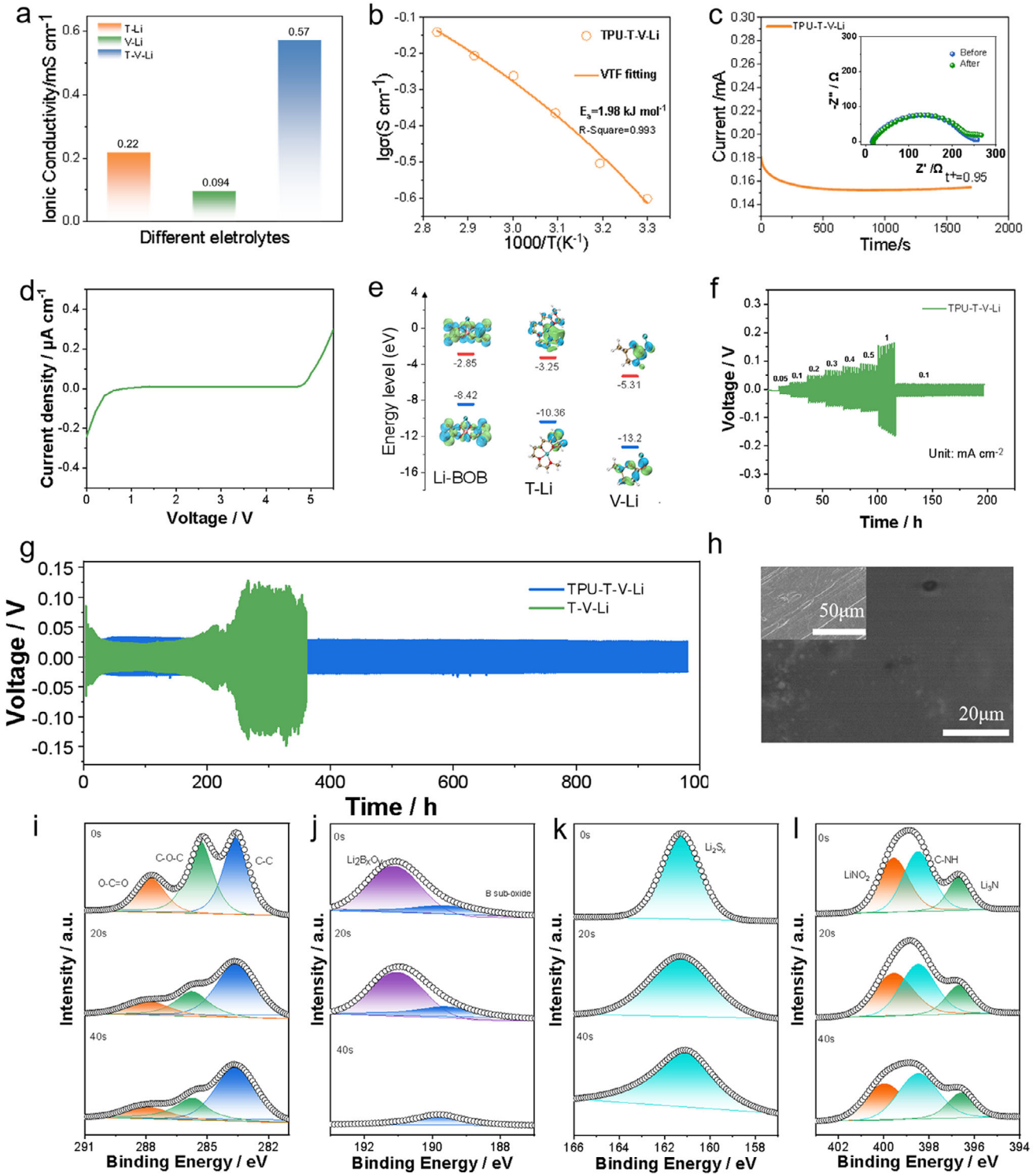

FIGURE 4 | Electrochemical performance, reversible lithium deposition, and SEI composition. (a) Room-temperature ionic conductivity of T-Li, V-Li, and T-V-Li. (b) Ionic conductivity vs. temperature of TPU-T-V-Li. (c) Chronoamperometry profile and EIS (inset) before and after polarization of Li|TPU-T-V-Li|Li cell. (d) LSV curve of TPU-T-V-Li. (e) HOMO and LUMO levels of LiBOB, T-Li, and V-Li. (f) Rate and (g) cycle performance of Li||Li cell using TPU-T-V-Li. SEM characterization of the (h) initial (internal illustration) and cycled Li. XPS of (i) C 1s, (j) B 1s, (k) S 2p, and (l) N 1s of cycled Li based on Li|TPU-T-V-Li|Li cell.

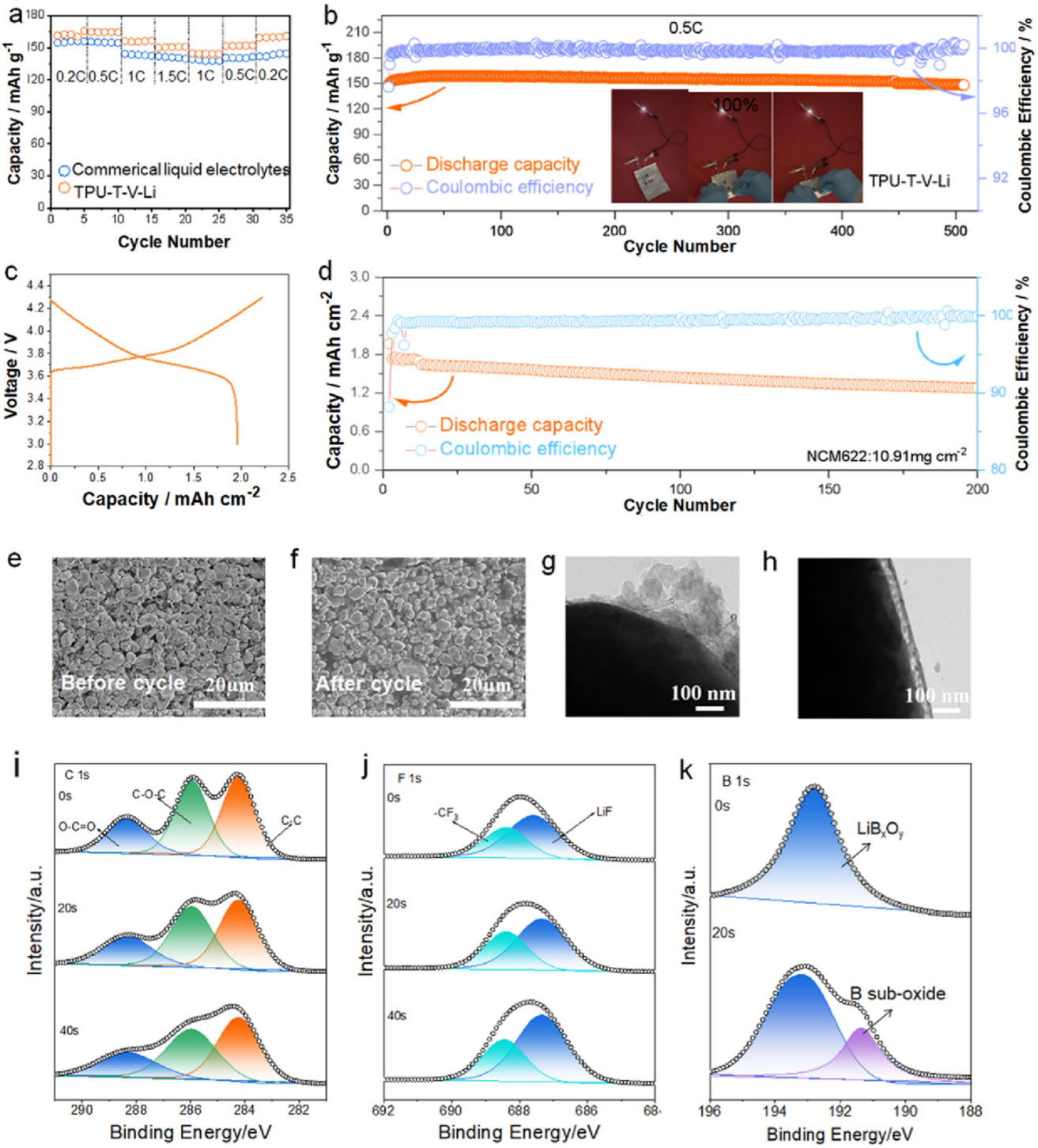

FIGURE 5 | Full-cell performance and cathode interface. (a) C-rate performance of Li||LFP cell using commercial liquid electrolyte and TPU-T-V-Li, respectively. (b) Long cycle performance of Li|TPU-T-V-Li|LFP cell. (c) Charging/discharging curves of Li|TPU T-V-Li|NCM622 cell under different cycles and (d) corresponding cycle performance. SEM images of (e) initial and (f) cycled NCM622. HR-TEM of cycled NCM622 using (g) commercial liquid electrolyte and h) TPU-T-V-Li, respectively. XPS of (i) C 1s, (j) F 1s, and (k) B 1s of cycled NCM622.

Figure 4f demonstrates that the polymer membrane-based Li||Li symmetric cell exhibits excellent cycling stability under varying current densities (0.05–1 mA cm^{-2}). Notably, while the T-V-Li electrolyte system experienced rapid microshorting at 0.1 mA cm^{-2}/0.1 mAh cm^{-2}, the polymer membrane-equipped Li||Li cells maintained stable cycling for ~1000 h (Figure 4g). This performance difference confirms the electrolyte membrane's dual capabilities: effective suppression of lithium dendrite growth and superior interfacial compatibility with the lithium metal anode. Post-cycle SEM analysis of the lithium metal surface revealed no noticeable protrusions (Figure 4h), further corroborating the polymer membrane's dendrite-inhibiting effect.

Detailed post-mortem analysis was conducted on both the surface and subsurface regions of cycled lithium metal [40, 41]. XPS characterizations (C 1s, B 1s, S 2p, and N 1s spectra in Figure 4i–l) demonstrate that the SEI layer formed on the lithium anode contains not only polymer-derived components but also inorganic species including borides (e.g., LiB_xO_y), sulfides (e.g., Li_2S_x), and nitrides (e.g., Li_3N). This multifunctional SEI composition synergistically ensures exceptional stability of the lithium metal anode during prolonged cycling, as validated by both electrochemical performance and surface morphology analysis.

The rate performance of Li||LFP cells using T-Li and T-V-Li is shown in Figure S16, further confirming the outstanding performance of T-V-Li. Figure 5a compares the C-rate performance of Li||LFP batteries fabricated with commercial liquid electrolyte and TPU-T-V-Li. The polymer electrolyte-based Li||LFP exhibits superior rate performance across various current densities, maintaining a discharge specific capacity of 150 mAh g^{-1} at 1.5 C, with corresponding charge–discharge curves shown in Figure S17. This improvement is attributed to the synergistic effects of T-V-Li's unique solvation structure and TPU's ion-conducting channels, which collectively reduce ionic migration barriers and facilitate rapid Li^+ transport. Remarkably, as shown in Figure 5b, the Li|TPU-T-V-Li|LFP solid-state battery achieves stable cycling over 500 cycles at 0.5 C, with an average capacity of 155 mAh g^{-1}, 99.9% Coulombic efficiency, and 99.7% capacity retention. Meanwhile, the corresponding flexible battery prepared with this electrolyte can enable the LED to work normally in both flat and bent states (inset of Figure 5b), confirming the potential of this electrolyte for application in flexible energy storage devices.

To further validate electrolyte practicality, we evaluated cycling performance using commercial high-loading (~12 mg cm^{-2}) LFP electrodes. Figure S18a presents the initial charge–discharge profile, while Figure S18b shows the cycling performance at 0.5 C, achieving an average areal capacity of 1.6 mAh cm^{-2} with 99.45% average coulombic efficiency about 150 cycles. Figure 5c displays charge–discharge curves for TPU-T-V-Li paired with high-loading NCM622, and Figure 5d shows corresponding long-term cycling, where the cell maintains 200 cycles with 1.6 mAh cm^{-2} average areal capacity and 99.4% average coulombic efficiency. SEM analysis reveals minimal morphological changes in NCM811 after cycling (Figure 5f) compared to the pristine state (Figure 5e). Notably, the polymer electrolyte-cycled NCM622 exhibits a uniform and thin CEI layer (Figure 5h), contrasting with the uneven, thick CEI components formed in the commercial liquid electrolyte system (Figure 5g). XPS characterization further confirms homogeneous distribution of organic components (e.g., from partial polymer decomposition, Figure 5i), inorganic fluorides (from binder evolution, Figure 5j), and inorganic borides (from LiBOB decomposition, Figure 5k) across the electrode surface. Moreover, we also confirmed that a pouch cell also achieves a capacity of 1600 mAh (Figure S19).

3 | Conclusion

In conclusion, the study introduces a fluorine-free electrolyte architecture with single-ion conduction characteristics that redefines high-energy lithium battery chemistry through engineered solvent-polymer elastic bridging interaction. By integrating a zwitterionic polyurethane matrix with an F-free LHCE (LiBOB containing tetraethylene glycol dimethyl ether and γ-valerolactone), the design achieves outstanding electrochemical performance: an extremely high lithium-ion transference number of 0.95, a high room-temperature ionic conductivity 1.3 mS cm^{-1}, and a high mechanical strength of 1.1 MPa. These advancements stem from selective LiBOB-solvent coordination and modulated polymer backbone interactions. Further combined with the formation of an inorganic boride-rich interfacial layer, this enables stable cycling of Li||Li cells (with plating/stripping lasting for 1000 h) and demonstrates exceptional full-cell performance (for example, achieving 99.4% capacity retention over 200 cycles for a high-loading NCM622 cathode). This molecular engineering strategy—particularly the solvent-polymer elastic bridging and solvation regulation—not only pioneers a sustainable pathway for fluorine-free lithium batteries but could also be extended to sodium- and potassium-ion systems by designing analogous conductors with tailored coordination environments. Moreover, the demonstrated mechanical robustness, self-healing capability, and interfacial stability offer a promising platform for developing safe, adaptable electrolytes in flexible and wearable electronics, underscoring its broader scientific and technological relevance.

Acknowledgements

We acknowledge financial support from the Funded by the Basic Research Program of Jiangsu (No. BK20243057), the National Key Research and Development Program of China (Nos. 2024YFB3612500, 2024YFB3612600 and 2023YFB3608904), the National Natural Science Foundation of China (Nos. 52533008, 21835003, U25A20628, 22561160129, 22479074, 22475096, 22402146 and 22572140), the Natural Science Foundation of Jiangsu Province (No. BK20210601 and BE2019120), the Program for Jiangsu Specially-Appointed Professor (No. RK030STP15001), the NUPT "1311 Project" and Scientific Foundation (Nos. NY219159 and NY219021), the Leading Talent of Technological Innovation of National Ten-Thousands Talents Program of China, the Excellent Scientific and Technological Innovative Teams of Jiangsu Higher Education Institutions (No. TJ217038), the Priority Academic Program Development of Jiangsu Higher Education Institutions (Nos. PAPD and YX030003), the China Postdoctoral Science Foundation (No. 2023M741624), the Project of State Key Laboratory of Organic Electronics and Information Displays, NJUPT (No. GZR2023010016), the Natural Science Foundation of NJUPT (Nos. NY223079 and NY224119), the Equipment Pre-Research and Ministry of Education Joint Fund (No. 8091B02052407), the Fundamental Research Program Key Project of Jiangsu Province (No. BK20253008), the Science and Technology Major Project of Jiangsu Province (No. BG2024013), the Scientific and Technological Achievements Transformation Special Fund of Jiangsu Province (No. BA2023037), the Academic Degree and Postgraduate Education Reforming Project of Jiangsu Province (No. JGKT24_C001), the Key Core Technology Open Competition Project of Suzhou City (No. SYG2024122), the Open Research Fund of Suzhou Laboratory (No. SZLAB-1308-2024-TS005), and the Chenzhou National Sustainable Development Agenda Innovation Demonstration Zone Provincial Special Project (No. 2023sfq11).

Conflicts of Interest

The authors declare no conflicts of interest.

Data Availability Statement

The data that support the findings of this study are available from the corresponding author upon reasonable request.

References

1. J. Fan, C. Liu, N. Li, et al., "Wireless Transmission of Internal Hazard Signals in Li-Ion Batteries," *Nature* 641 (2025): 639–645, https://doi.org/10.1038/s41586-025-08785-7.

2. S. Wang, S. Xiao, S. Li, et al., "Organic Cationic-Coordinated Perfluoropolymer Electrolytes with Strong Li^+-Solvent Interaction for Solid-State Li-Metal Batteries," *Angewandte Chemie International Edition* 63 (2024): 202412434, https://doi.org/10.1002/anie.202412434.

3. L. Zhang, S. Wang, Q. Wang, H. Shao, and Z. Jin, "Dendritic Solid Polymer Electrolytes: A New Paradigm for High-Performance Lithium-Based Batteries," *Advanced Materials* 35 (2023): 2303355, https://doi.org/10.1002/adma.202303355.

4. H. Huang, Y. Hu, Y. Hou, et al., "Delocalized Electrolyte Design Enables 600 Wh kg^{-1} Lithium Metal Pouch Cells," *Nature* 644 (2025): 660–667, https://doi.org/10.1038/s41586-025-09382-4.

5. C. M. Efaw, Q. Wu, N. Gao, et al., "Localized High-Concentration Electrolytes Get More Localized Through Micelle-Like Structures," *Nature Materials* 22 (2023): 1531–1539.

6. Z. Jiang, C. Li, T. Yang, et al., "Fluorine-Free Lithium Metal Batteries with a Stable LiF-Free Solid Electrolyte Interphase," *ACS Energy Letters* 9 (2024): 1389–1396, https://doi.org/10.1021/acsenergylett.3c02724.

7. S. Wang, L. Zhang, Z. Hu, et al., "Intrinsic Structural and Coordination Chemistry Insights of Li Salts in Rechargeable Lithium Batteries," *Advanced Materials* 37 (2025): 2420428, https://doi.org/10.1002/adma.202420428.

8. E. S. Flitz, N. R. Singstock, S.-B. Son, et al., "A Low-Cost, Fluorine-Free Electrolyte for Improved Sodium Batteries," *Joule* 9 (2025): 102045, https://doi.org/10.1016/j.joule.2025.102045.

9. S. Wang, S. Xiao, H. Cai, et al., "Elastic Polymer Electrolytes Integrated With In Situ Polymerization-Transferred Electrodes Toward Stretchable Batteries," *ACS Energy Letters* 9 (2024): 3672–3682, https://doi.org/10.1021/acsenergylett.4c01254.

10. Q. Wang, P. Zou, L. Ren, et al., "Ultrathin Composite Li Electrode for High-Performance Li Metal Batteries: A Review From Synthetic Chemistry," *Advanced Functional Materials* 33 (2023): 2213648, https://doi.org/10.1002/adfm.202213648.

11. P. Karanth, M. Weijers, A. K. Lavrinenko, et al., "Designing Fluorine-Free Electrolytes for Lithium Metal Batteries," *Journal of the American Chemical Society* 147 (2025): 46008–46022, https://doi.org/10.1021/jacs.5c12584.

12. C. Liu, T. Yang, Q. Yu, et al., "High-Voltage Fluoride-Free Electrolytes for Ni-Rich Cathodes Offering Superior Water Resistance," *ACS Sustainable Chemistry & Engineering* 13 (2025): 8951–8958, https://doi.org/10.1021/acssuschemeng.5c00933.

13. A. Kushwaha, S. Bhakta, M. Ahmed, et al., "Dual Fluorine-Free Salt Electrolytes for Medium-to-High Voltage Lithium Metal Batteries," *Journal of Power Sources* 667 (2026): 239241, https://doi.org/10.1016/j.jpowsour.2025.239241.

14. C. Liu, K. Ren, S. Wu, et al., "Reevaluating the Effect of a LiF-Containing Solid Electrolyte Interphase on Lithium Metal Anodes," *Nano Letters* 25 (2025): 7762–7769, https://doi.org/10.1021/acs.nanolett.5c00675.

15. Y. Shuai, Y. Hu, X. Gong, et al., "Fluorine-Free Electrolytes for High-Performance and Low-Cost Lithium Metal Batteries," *Chemical Engineering Journal* 505 (2025): 159101, https://doi.org/10.1016/j.cej.2024.159101.

16. S. Wang, Q. Li, H. Gao, et al., "A Polyzwitterion-Mediated Polymer Electrolyte With High Oxidative Stability for Lithium-Metal Batteries," *Small* 19 (2023): 2304677, https://doi.org/10.1002/smll.202304677.

17. T. Hou, D. Wang, B. Jiang, et al., "Ion Bridging Enables High-Voltage Polyether Electrolytes for Quasi-Solid-State Batteries," *Nature Communications* 16 (2025): 962, https://doi.org/10.1038/s41467-025-56324-9.

18. C. Lu, H. Jiang, X. Cheng, et al., "High-Performance Fibre Battery with Polymer Gel Electrolyte," *Nature* 629 (2024): 86–91, https://doi.org/10.1038/s41586-024-07343-x.

19. S.-M. Hao, J. Zhu, S. He, et al., "Water-in-Polymer Electrolyte with a Wide Electrochemical Window and Recyclability," *Nature Sustainability* 7 (2024): 661–671, https://doi.org/10.1038/s41893-024-01327-5.

20. P. Chen, S. Liu, H. Zhou, et al., "Closed-Loop Recyclable Solid-State Polymer Electrolytes Enabled by Reversible Lithium Salt Catalysis," *Journal of the American Chemical Society* 147 (2025): 7624–7633, https://doi.org/10.1021/jacs.4c17035.

21. C. Liu, S. Wang, X. Wu, et al., "In Situ Construction of Zwitterionic Polymer Electrolytes with Synergistic Cation–Anion Regulation Functions for Lithium Metal batteries," *Advanced Functional Materials* 34 (2023): 2307248.

22. S. Wang, L. Zhang, Q. Zeng, et al., "Designing Polymer Electrolytes via Ring-Opening Polymerization for Advanced Lithium Batteries," *Advanced Energy Materials* 14 (2024): 2302876, https://doi.org/10.1002/aenm.202302876.

23. N. J. Shah, C. Fang, N. C. Osti, et al., "Nanosecond Solvation Dynamics in a Polymer Electrolyte for Lithium Batteries," *Nature Materials* 23 (2024): 664–669, https://doi.org/10.1038/s41563-024-01834-y.

24. L. Xu, X. Xiao, H. Tu, et al., "$LiNO_3$-Based Electrolytes via Electron-Donation Modulation for Sustainable Nonaqueous Lithium Rechargeable Batteries," *Advanced Materials* 35 (2023): 2303193, https://doi.org/10.1002/adma.202303193.

25. L. Zou, K. Shi, H. Liu, et al., "Polybenzimidazole-Reinforced Polyethylene Oxide-Based Polymer-in-Salt Electrolytes Enabling Excellent Structural Stability and Superior Electrochemical Performance for Lithium Metal Batteries," *Chemical Engineering Journal* 465 (2023): 142794, https://doi.org/10.1016/j.cej.2023.142794.

26. G. M. Hobold, C. Wang, K. Steinberg, Y. Li, and B. M. Gallant, "High Lithium Oxide Prevalence in the Lithium Solid–Electrolyte Interphase for High Coulombic Efficiency," *Nature Energy* 9 (2024): 580–591, https://doi.org/10.1038/s41560-024-01494-x.

27. H. Chen, K. Chen, L. Luo, et al., "$LiNO_3$-Based Electrolytes via Electron-Donation Modulation for Sustainable Nonaqueous Lithium Rechargeable Batteries," *Angewandte Chemie International Edition* 63 (2024): 202316966, https://doi.org/10.1002/anie.202316966.

28. H. Zhang, X. Judez, A. Santiago, et al., "Fluorine-Free Noble Salt Anion for High-Performance All-Solid-State Lithium–Sulfur Batteries," *Advanced Energy Materials* 9 (2019): 1900763, https://doi.org/10.1002/aenm.201900763.

29. J. Li, J. Yang, Z. Ji, et al., "Prospective Application, Mechanism, and Deficiency of Lithium Bis(oxalate)Borate as the Electrolyte Additive for Lithium-Batteries," *Advanced Energy Materials* 13 (2023): 2301422, https://doi.org/10.1002/aenm.202301422.

30. X. He, B. Yan, X. Zhang, et al., "Fluorine-Free Water-in-Ionomer Electrolytes for Sustainable Lithium-Ion Batteries," *Nature Communications* 9 (2018): 5320.

31. K. S. Teoh, M. Melchiorre, S. Darlami Magar, et al., "Fluorine-Free Lithium-Ion Capacitor With Enhanced Sustainability and Safety Based on Bio-Based γ-Valerolactone and Lithium Bis(Oxalato)Borate Electrolyte," *Advanced Materials* 36 (2024): 2310056, https://doi.org/10.1002/adma.202310056.

32. F. A. Kreth, L. Köps, C. Leibing, et al., "Enabling Fluorine-Free Lithium-Ion Capacitors and Lithium-Ion Batteries for High-Temperature Applications by the Implementation of Lithium Bis(oxalato)Borate and Ethyl Isopropyl Sulfone as Electrolyte," *Advanced Energy Materials* 14 (2024): 2303909, https://doi.org/10.1002/aenm.202303909.

33. M. A. Navarra, A. Tsurumaki, F. M. Vitucci, A. Paolone, O. Palumbo, and S. Panero, "A Novel Li^+-Conducting Polymer Membrane Gelled by Fluorine-Free Electrolyte Solutions for Li-Ion Batteries," *Batteries & Supercaps* 3 (2020): 1112–1119, https://doi.org/10.1002/batt.202000078.

34. J. Huang, G. Rui, Y. Yan, et al., "Fluorine-Free Strongly Dipolar Polymers Exhibit Tunable Ferroelectricity," *Science* 389 (2025): 69–72, https://doi.org/10.1126/science.ads4702.

35. K. Wang, V. Koverga, N. Maslekar, et al., "Novel Zwitterionic Polyurethane-in-Salt Electrolytes with High Ion Conductivity, Elasticity, and Adhesion for High-Performance Solid-State Lithium Metal Batteries," *Advanced Energy Materials* 15 (2025): 2405676, https://doi.org/10.1002/aenm.202405676.

36. M. J. Lee, J. Han, K. Lee, et al., "Elastomeric Electrolytes for High-Energy Solid-State Lithium Batteries," *Nature* 601 (2022): 217–222, https://doi.org/10.1038/s41586-021-04209-4.

37. J. Han, M. J. Lee, K. Lee, et al., "Role of Bicontinuous Structure in Elastomeric Electrolytes for High-Energy Solid-State Lithium-Metal Batteries," *Advanced Materials* 35 (2023): 2205194, https://doi.org/10.1002/adma.202205194.

38. S. Li, H. Hong, X. Yang, et al., "In Situ Polymerized Polyfluorinated Crosslinked Polyether Electrolytes for High-Voltage Lithium Metal Batteries," *Advanced Materials* 37 (2025): 2504333, https://doi.org/10.1002/adma.202504333.

39. Y. Nie, D. Luo, T. Yang, et al., "Ultrathin Electrolyte Membranes with Reinforced Concrete Structure for Fast-Charging Solid-State Lithium Metal Batteries," *Advanced Materials* 37 (2025): 2504092, https://doi.org/10.1002/adma.202504092.

40. C. Ma, C. Koroni, J. Hu, J. Qian, G. Han, and H. Xiong, "Nanoreactor-Structured Defective MoS_2: Suppressing Intercalation-Induced Phase Transitions and Enhancing Reversibility for Potassium-Ion Batteries," *Nano-Micro Letters* 18 (2026): 138, https://doi.org/10.1007/s40820-025-01992-x.

41. X. Zhang, Y. Fan, H. Li, et al., "Phase-Reconstructable MoS_2 Heterostructures for High-Performance Sodium-Ion Batteries," *ACS Energy Letters* 11 (2025): 925–935, https://doi.org/10.1021/acsenergylett.5c03845.

Supporting Information

Additional supporting information can be found online in the Supporting Information section.

Supporting File: adma72977-sup-0001-SuppMat.docx.